

Small, Electron-Donating Substituents Give CO₂ Activation by Permethylpentalene Zirconium Amido Complexes the Upper Hand: A DFT Study of Distortion and Interaction

Daniel Chabeda, H. Ray Kelly, Patrick L. Holland, and Victor S. Batista*



Cite This: *Inorg. Chem.* 2023, 62, 3000–3006



Read Online

ACCESS |



Metrics & More

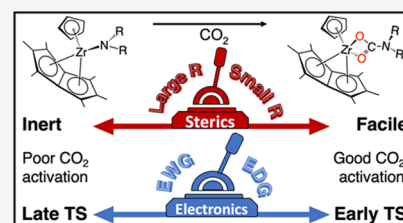


Article Recommendations



Supporting Information

ABSTRACT: An insight into factors controlling CO₂ activation is necessary to develop molecular systems that utilize CO₂ as a chemical feedstock. Two permethylpentalene zirconium cyclopentadienyl (mono)amido complexes, Pn*ZrCp(NR₂), were previously assessed for CO₂ activation, and a strong dependence on the amido substituent was observed. The R = Me analogue reacted rapidly and quantitatively at room temperature to form the carbamate complex, while the R = Ph species was inert. Here, we investigate the origin of this reactivity difference using DFT and the distortion–interaction model to characterize steric and electronic contributions to the activation barrier. We find that the barrier for CO₂ insertion with R = Me (19.1 kcal/mol) is lower than with R = Ph (36.6 kcal/mol), explaining the inertness of the Ph-substituted analogue. The distortion energy trend follows the steric bulk of the amido substituents, and the bulkier Ph-substituted complex has a consistently higher distortion energy along its potential energy surface than that of the Me-substituted complex. The interaction energy trend follows the electronics, and a more electron-donating Me-substituted complex shows a consistently lower interaction energy. The balance of these effects at the corresponding TS gives a reduced activation barrier. Small, electron-donating substituents therefore facilitate CO₂ activation in these complexes.



INTRODUCTION

The adverse environmental impacts of the increase in atmospheric carbon dioxide (CO₂) concentrations have motivated efforts to develop molecular systems which capture CO₂ to make value-added compounds.^{1–5} Carbamates are prime examples of CO₂-derived compounds which find use in agrochemical, synthetic, and pharmaceutical products such as fungicides, polycarbonate plastics, and peptide surrogates in drugs.^{5–9} The main challenge to carbamate synthesis is the thermodynamic stability and kinetic inertness of CO₂, so gaining an understanding of the factors that control CO₂ activation is of interest to sustainability goals.^{10,11} A recent work by the O'Hare group has demonstrated the reactivity of permethylpentalene (η^8 -C₈Me₆ = Pn*) zirconium cyclopentadienyl (mono)amido complexes toward CO₂ activation, producing novel zirconium Pn* carbamate complexes.⁷ Intriguingly, two analogous Pn*ZrCp(NR₂) (PnZr) complexes **1a**, R = Me, and **1b**, R = Ph (Figure 1), showed drastically different reactivities toward CO₂ activation. Methyl-substituted

amido complex **1a** reacted with CO₂ to quantitatively form the carbamate complex at room temperature, while phenyl-substituted **1b** exhibited no reactivity toward CO₂ activation even after heating at 75 °C for 16 h.⁷

The observed substituent-dependent reactivity was rationalized in terms of the lower Lewis basicity of HNPh₂ compared to HNMe₂ due to the electron-withdrawing Ph substituent and the increased steric congestion around the Zr–N bond in **1b**.⁷ However, theoretical/computational studies that could provide a fundamental understanding and guide the design of improved CO₂ activation by Zr and other group 4 metal catalysts have yet to be reported.

Here, we use the distortion–interaction, or activation strain, method to analyze molecular contributions to reaction barriers by leveraging the high degree of atomistic manipulation provided by computational techniques.^{12–17} Species along the potential energy surface (PES) of a relevant transition state (TS) are partitioned into fragments to quantify the contribution of specific chemical regions to the overall reactivity (Figure 2). The quantities computed along the PES are the distortion (activation strain) and interaction

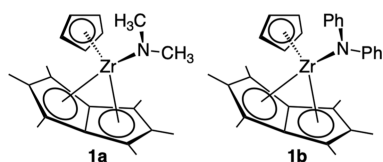
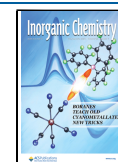


Figure 1. Pn*ZrCp(NR₂) complexes **1a** and **1b**.

Received: October 5, 2022

Published: February 8, 2023



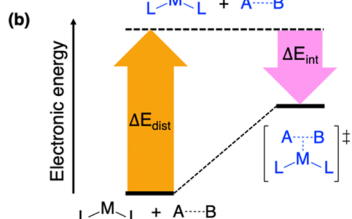
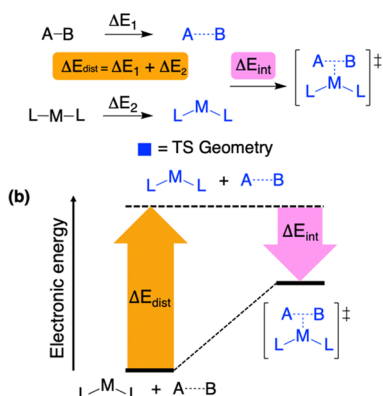
(a) Overall Reaction: $L-M-L + A-B \rightarrow ABML_2$ 

Figure 2. Distortion–interaction method visualized in a (a) stepwise fashion and (b) as an energy diagram. The stepwise representation shows the distortion of the separate intermediates (black) into their TS geometries (blue) and combination to form the TS. The energy diagram depicts how the energies of the intermediates, TS fragments, and TSs are related through ΔE_{dist} (orange) and ΔE_{int} (pink).

energies. The distortion energy, ΔE_{dist} , is the energy required to deform the starting geometry as it progresses along the reaction path. ΔE_{dist} can be broken down into individual contributions from each fragment (e.g., gray and orange in Figure 4) to understand the molecular-level structural changes influencing the activation barrier. Steric and electronic factors impact ΔE_{dist} including the force constants of bonds which must deform, the size of the substituents, and how the deformations change the bonding orbital overlap. The interaction energy, ΔE_{int} , reports the stabilization from combining the increasingly deformed fragments into their linked geometry along the PES. It is also influenced by the steric and electronic properties of the fragments such as the electron-withdrawing/-donating ability, charge distribution, and bonding capabilities due to the steric bulk.¹² The total energy along the PES is the sum of distortion and interaction energies, so analysis of distortion and interaction unlocks insights into the parameters controlling the behavior of the reactions.

The distortion–interaction method is particularly useful in cases where a limited molecular modification induces a drastic behavioral change,¹² such as the reactivity difference between close analogues **1a** and **1b**. To study this reactivity difference, a plausible rate-limiting step for CO₂ activation by Pn*Zr complexes must first be identified. The corresponding TS defines the activation energy and provides a quantitative indicator of reactivity.

Mechanistic investigations of CO₂ activation have been reported extensively in the literature.^{2,18–26} Due to its thermodynamic stability, CO₂ is a poor ligand for low-valent transition metals. Pathways for CO₂ activation that involve low-valent metal centers usually do not involve pre-activation through a metal–CO₂ adduct.^{1,18,19} The most common pathway supported by computational investigations to date for CO₂ insertion into metal–heteroatom bonds is through the nucleophilic attack of a nitrogen lone pair on the CO₂ carbon.^{18,27} Therefore, we explored that mechanism in our computational analysis.

COMPUTATIONAL METHODS

DFT calculations were performed using Gaussian 16, Revision C.01.²⁸ The default convergence criteria and integration grid were used for calculations of thermodynamic and electronic properties of the molecules. Benchmarking was performed with combinations of the PBE,²⁹ B3LYP,^{30–32} and ω B97X-D³³ functionals with double-zeta Pople and correlation-consistent basis sets on nonmetal atoms and the DEF2SVP basis set³⁴ with its effective core potential (ECP) on Zr. D3 empirical dispersion with Becke–Johnson damping^{35,36} was included in the PBE and B3LYP models to capture the effects of noncovalent interactions on the aromatic ligands. Ultimately, the B3LYP functional with the 6-31G(d)^{37–39} basis set on nonreactive nonmetal atoms, 6-31+G(d)⁴⁰ on reactive atoms (amido nitrogen and CO₂), and DEF2SVP with its ECP⁴¹ on Zr (Figure S1) were chosen because of good agreement between the optimized geometries and experimental X-ray data for complex **1a** (see Supporting Information Section S1 for benchmarking results).⁷ Thermodynamic values were computed from the optimized gas-phase geometries, and all minima were assessed through normal mode analysis.

After geometry optimization, single-point energy calculations were performed using the 6-311G(2df,p)⁴² basis set on nonreactive atoms, 6-311+G(2df,p)⁴³ on the reactive atoms, and the def2-TZVP⁴⁴ basis set with an ECP on Zr. Solvation with PCM^{45,46} benzene was included in single-point calculations to incorporate the effect of the experimental solvent environment. Electronic energies from the triple-zeta level were combined with the thermal corrections from frequency calculations at the double-zeta level to obtain the reported free energies. Benchmarking of optimizations with PCM and SMD solvent models showed only small changes to the structures and distortion–interaction energies (Table S2, Figure S2).

The distortion–interaction energies were calculated as solvated single points at the triple zeta level using geometries optimized at the double zeta level. The intrinsic reaction coordinate (IRC) was computed at the double zeta level using a 0.05 Bohr step size until default termination at a gradient inflection point, and subsequent single point energies at the triple zeta level were calculated on the geometries from each IRC step for the distortion–interaction analysis. All distortion–interaction values are electronic energies because the TS fragments are not at an energy minimum and thus normal mode analysis would be inappropriate; enthalpies and free energies are thus inaccessible for the distortion–interaction analysis. The CMS partial atomic charges⁴⁷ were obtained by electronic population analysis based on the Hirshfeld method.⁴⁸

RESULTS

Figure 3 shows the reaction free energy profile computed for CO₂ insertion. Direct nucleophilic attack of the amido ligand onto CO₂ and pre-activation of the CO₂ on Zr were both considered, but extensive exploration of metal–CO₂ adduct geometries did not yield stable intermediates along the pre-activation pathway. Thus, we proceeded with the direct nucleophilic attack mechanism where the electron-rich nitrogen donates electron density to CO₂, forming the carbamate intermediate. Insertion of CO₂ into the Zr–N bond forms an η^2 intermediate, **2**, with the N and O of the carbamate coordinated to Zr. At this step, a difference appears between Me and Ph complexes: while Me-substituted **2a** is the product of the TS1a IRC pathway, the analogous species at the end of the TS1b coordinate fails to minimize to a stable N- and O-bound η^2 intermediate. Optimization of the TS1b IRC endpoint consistently yields the stable η^2 complex **3** with coordinating carbamate oxygens, even if a very small 0.01 Bohr optimization step is used with full Hessian calculations performed at each step. The energy gap between TS1b and the IRC endpoint was compared to the difference in TS1a and **2a**. The Ph endpoint structure (Figure S3) is less stabilized by 8 kcal/mol compared to **2a**; its energy is closer to that of the

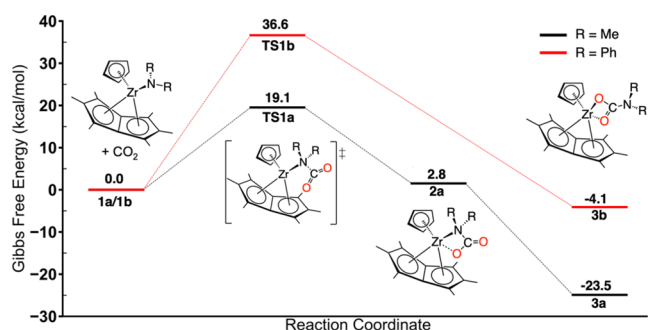


Figure 3. Free energy landscape for selected intermediates and TS along the proposed CO_2 insertion pathway for PnZr complexes. Values marked a and b correspond to Gibbs free energies calculated for the R = Me and R = Ph analogues, respectively. The reaction from 1 to 3 is more thermodynamically favorable for the R = Me amido complex than for R = Ph, $\Delta G = -23.5$ and -4.1 kcal/mol respectively. In addition, series a has a lower activation barrier than series b, with $\Delta G^\ddagger = 19.1$ and 36.6 kcal/mol, respectively.

TS. We conclude that species **2b** is unstable and suggest a pathway that proceeds directly from **1b** to **3b** through **TS1b**.

Experimental spectroscopic data suggest an intermediate η^1 , O-bound carbamate complex $\text{Pn}^*\text{Zr}(\eta^1\text{-O}_2\text{CNMe}_2)$, which is not found by DFT calculations of the isolated complex. CO_2 activation has been shown to be sensitive to the coordination mode of supporting ligands,^{49,50} so optimizations with η^5 Pn* coordination were attempted, but the species reorganizes to an η^8 Pn* and no η^1 carbamate could be optimized. The η^1 species might not have been the minimum energy structure because the calculations only consider an isolated molecule. The O-bound η^2 species was found to be lower in energy at all levels of theory.

Figure 3 shows that the reaction from **1** to **3** is more thermodynamically favorable for the R = Me amido complex **1a**, $\Delta G = -23.5$ kcal/mol, than for the R = Ph complex **1b**, $\Delta G = -4.1$ kcal/mol. In addition, **1a** traverses a lower activation barrier than **1b**, with $\Delta G^\ddagger = 19.1$ and 36.6 kcal/mol, respectively. Therefore, it is expected that the reaction of **1a** with CO_2 would occur rapidly and quantitatively at room temperature, whereas the reaction with **1b** would be extremely slow, consistent with experimental observations.⁷

Distortion–Interaction Analysis. We conduct this analysis in steps, first as a limited analysis at the TS and then along the entire PES. The distortion energy, ΔE_{dist} , quantifies the degree of deformation the starting geometry must feel to achieve the TS conformation (**Figure 4**). The smaller ΔE_{dist} of **TS1a** compared to **TS1b** ($\Delta\Delta E_{\text{dist}} = -17.1$ kcal/mol) demonstrates that methyl groups induce less deformation to the complex at the TS and quantifies the relative stabilization. Below, we will rationalize why this is the case.

The relative contribution of each reactant fragment to ΔE_{dist} shows that distortions of the **1a** and **1b** ligand frameworks make up 58 and 63% of the energy contribution to **TS1a** and **TS1b**, respectively (**TS1a**: 11.4 kcal/mol; **TS1b**: 24.3 kcal/mol). The contribution of CO_2 deformation to the distortion energy is complementary. A direct comparison of the distortion energies reveals an interesting asymmetry: the deformed CO_2 in phenyl-substituted **TS1b** (12.6 kcal/mol) is higher in energy than the corresponding fragment in methyl-substituted **TS1a** (8.4 kcal/mol). Similarly, the contribution of the **1b** fragment to the barrier (24.3 kcal/mol) is greater than

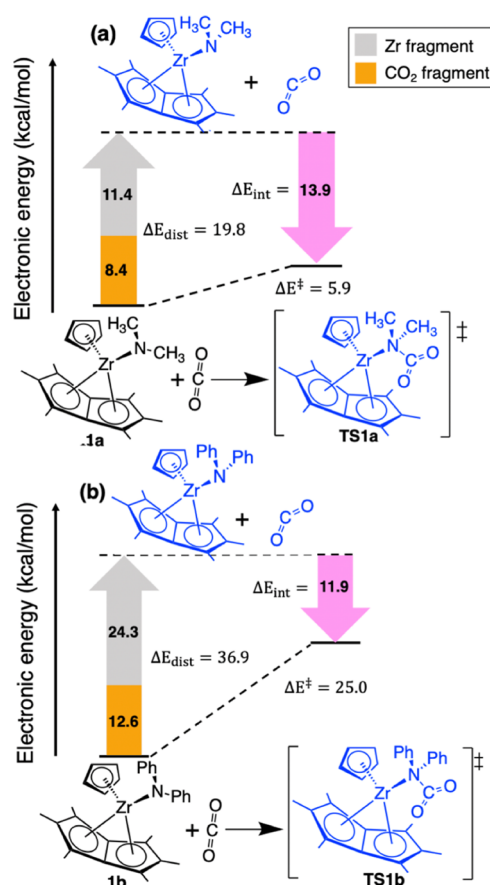


Figure 4. Distortion–interaction diagrams for (a) **TS1a** and (b) **TS1b**. The distortion energy is 19.8 kcal/mol for **TS1a** and 36.9 kcal/mol for **TS1b**, producing a relative $\Delta\Delta E_{\text{dist}}$ of 17.1 kcal/mol (electronic energy). Species marked in blue retain the TS geometry.

that of the **1a** fragment (11.4 kcal/mol). The greater contribution of R = Ph fragments to ΔE_{dist} implies that the TSs are fundamentally different for R = Ph and R = Me complexes, with the phenyl-substituted pathway including a greater distortion penalty for deformation of the reactant geometry; this is consistent with **TS1b** appearing later on the PES than **TS1a**.

The interaction energy, ΔE_{int} , for recombining the TS fragments is slightly larger for the R = Me analogue **1a** (-13.9 kcal/mol) than for **1b** (-11.9 kcal/mol), indicating that, at the TS, the **TS1a** analogue has stronger interactions between $\text{Pn}^*\text{ZrCp}(\text{NR}_2)$ and CO_2 fragments. In other words, substituent modification from Me to Ph impairs bonding of the amido nitrogen with CO_2 . This trend is expected since the electron-donating nature of methyl enables a more facile nucleophilic attack from the **1a** nitrogen. Overall, the interaction energy at the TS shows a less dramatic shift between substituents, but no conclusion about the preeminence of distortion or interaction can be made without examining the entire PES. Before this analysis, we introduce two new complexes to complete the substituent character profile.

Distinguishing Steric from Electronic Effects. To examine the competing influence of steric and electronic effects, the PES for amido complexes **1c** and **1d** were computed, analogues with small, electron-withdrawing and

large, less electron-withdrawing substituents, respectively (Figure 5).

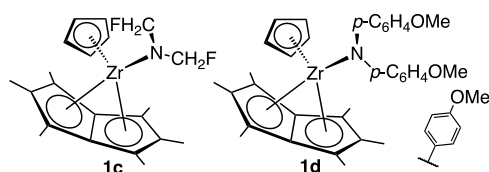


Figure 5. $\text{Pn}^*\text{ZrCp}(\text{NR}_2)$ analogues **1c** and **1d** were used to examine the competing effects of sterics and electronics on the barrier of CO_2 activation.

Complex **1c** is substituted with $\text{R} = \text{CH}_2\text{F}$, which is sterically similar to Me but is more electron-withdrawing due to the electronegative F atom. The activation barrier starting from **1c** is 27.1 kcal/mol, which is 8.0 kcal/mol greater than from the more electron-donating **1a** ($\Delta G^\ddagger = 19.1$ kcal/mol), so the electron-withdrawing group (EWG) slows the reaction. Complex **1d** is substituted with $\text{R} = 4\text{-C}_6\text{H}_4\text{OMe}$, which is sterically similar to Ph and but more electron-donating due to the para methoxy group. The activation barrier of **1d** is 31.7 kcal/mol, which is 4.9 kcal/mol less than that of the similarly large, more electron-withdrawing Ph complex **1b** ($\Delta G^\ddagger = 36.6$ kcal/mol). The distortion–interaction analysis at the TS for these complexes is shown in Figure S4.

Full Distortion Interaction Diagram. To accurately assess contributions to the reactivity difference, the distortion–interaction analysis was calculated for each step along an IRC coordinate. Figure 6 shows the corresponding distortion–interaction diagram with the IRC projected onto a relevant geometric parameter, the $\text{N}-\text{CO}_2$ bond length. The distortion energies represented by the upper dotted curves increase from left to right as the distinct reactants (long $\text{N}-\text{CO}_2$ bond distances) mutually orient to form the carbamate complex. The distortion energies show systematically larger values for larger amido substituents and similar values for groups with similar steric profiles, $\text{Ph} \sim 4\text{-C}_6\text{H}_4\text{OMe} > \text{Me} \sim \text{CH}_2\text{F}$. Notice that the distortion curves for the small substituents originate around 3.25 Å with values near the reference energy of unassociated PnZr and CO_2 , while the $\text{Ph}/4\text{-C}_6\text{H}_4\text{OMe}$ curves originate around 3.7 Å with a distortion energy of ~ 10 kcal/mol. All IRC trajectories terminated naturally at the PES inflection point, so this result indicates that the additional steric bulk of the $\text{Ph}/4\text{-C}_6\text{H}_4\text{OMe}$ substituents causes the complex to feel the CO_2 approach from much further and deform much earlier than for $\text{Me}/\text{CH}_2\text{F}$. Which deformations are occurring in this region? Changes to the total angle around the $\text{Ph}/4\text{-C}_6\text{H}_4\text{OMe}$ amido nitrogen show that deformation from trigonal planar to pyramidal amido binding occurs, as the total angle goes from $359.3^\circ/359.4^\circ$ to $357.1^\circ/357.2^\circ$ for $\text{N}-\text{CO}_2$ distances between 3.57 Å/3.74 Å and 2.98 Å/3.19 Å. This transition from planar to pyramidal binding results in the loss of aromaticity in the aromatic rings and a high energetic cost (see Supporting Information Section S4).

The interaction energies shown in Figure 6b decrease from left to right as the deformed fragments exhibit greater mutual interaction. There is a systematic lowering of interaction energies for more electron-donating substituents, $\text{Me} < 4\text{-C}_6\text{H}_4\text{OMe} \sim \text{Ph} < \text{CH}_2\text{F}$, corresponding to more fragment stabilization in the combined geometry along the PES. These

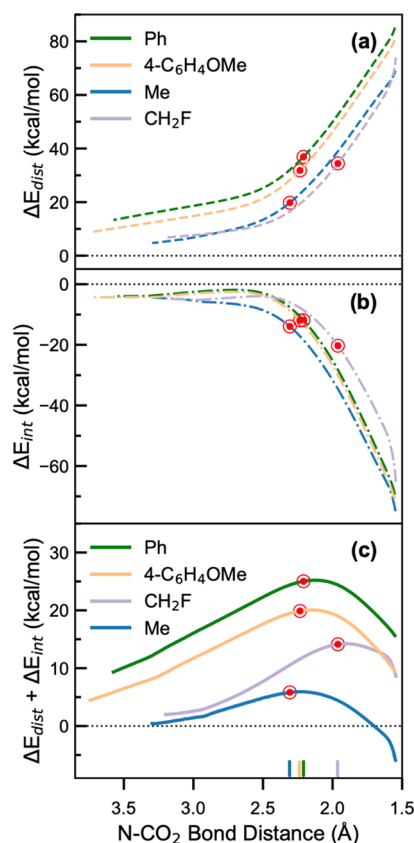


Figure 6. Distortion–interaction diagrams of TS1a-d along their respective reaction coordinates. The upper dashed traces (a) are distortion energies, the lower dash-dotted traces (b) interaction energies, and the solid lines (c) are the PES manifest from their sum. The circled red dots and color-coded tick marks show the location of the respective TS: Me (2.31 Å), $4\text{-C}_6\text{H}_4\text{OMe}$ (2.23 Å), Ph (2.21 Å), and CH_2F (1.96 Å). The PES for $\text{R} = \text{Me}$ (blue), Ph (green), CH_2F (lilac), and $4\text{-C}_6\text{H}_4\text{OMe}$ (orange) shows TS locations slightly shifted from the curve maxima. This is because the geometries of the IRC were calculated at the double zeta level while the plots are triple zeta energies. The electronic energies are referenced to the energies of free CO_2 plus **1a–d**, respectively. At long $\text{N}-\text{CO}_2$ bond lengths (left), the two reactants are separated, with little distortion or interaction. As the reactants come together, the distortion energy increases and the interaction energy decreases. The bulkier substituents show systematically larger distortion energies, $\text{Ph} \sim 4\text{-C}_6\text{H}_4\text{OMe} > \text{Me} \sim \text{CH}_2\text{F}$, and the more EDGs have lower interaction energies $\text{Me} < 4\text{-C}_6\text{H}_4\text{OMe} \sim \text{Ph} < \text{CH}_2\text{F}$. The combination of these curves leads to the PES profiles shown in (c) with electronic energy barrier heights ordered $\text{Me} < \text{CH}_2\text{F} < 4\text{-C}_6\text{H}_4\text{OMe} < \text{Ph}$.

two trends provide the basis for understanding the different barriers for each substituent. Summing the distortion and interaction curves yields the PES, with the TS located at the point where the interaction energy achieves a balance with the distortion energy (i.e., ΔE_{int} begins to decrease faster than ΔE_{dist} increases). The combination of these effects produces a direct correlation between electron-withdrawing ability and TS lateness, Me ($\text{N}-\text{CO}_2$ distance at TS: 2.31 Å) $< 4\text{-C}_6\text{H}_4\text{OMe}$ (2.23 Å) $< \text{Ph}$ (2.21 Å) $< \text{CH}_2\text{F}$ (1.96 Å).

Thus, we can answer the central question of this analysis: why is the activation barrier higher for $\text{R} = \text{Ph}$ than for $\text{R} = \text{Me}$? First, the Ph complex is more destabilized by the approach of CO_2 than Me as indicated by the systematically higher distortion energy along the reaction coordinate (Figure

6a, green). Second, the Ph complex has a more electron-withdrawing amido substituent, leading to a shallower interaction energy curve. The combination of increased distortion and lessened interaction shifts the balance point later along the reaction coordinate where the sum of distortion and interaction is larger: a larger activation barrier.

Additional insights come from the test in which amido ligands with a small, EWG and large, more electron-donating groups (EDGs) were used. The distortion curves overlap to within ~ 3 kcal/mol for the substituents of similar steric bulk such as Me and CH_2F . However, for those two complexes, the distortion energies at their respective TS are different by ~ 10 kcal/mol due to the change in TS lateness induced by the more electron-withdrawing CH_2F group; the later TS of CH_2F is the reason why such a small substituent has a larger distortion energy at its TS and a higher activation barrier. The N–CO₂ bond distance is 0.35 Å shorter and the free energy barrier ~ 10 kcal/mol higher in TS1c. Notice that without performing the distortion–interaction analysis along the entire reaction coordinate, we would have erroneously concluded that the higher CH_2F barrier compared to Me primarily arises from a greater distortion energy associated with deformation of the complex; the values of distortion for CH_2F (34.4 kcal/mol) are ~ 15 kcal/mol larger than for Me (19.8 kcal/mol) at their respective TS, while the interaction energies (-13.9 and -20.0 , respectively) are separated by only 6.1 kcal/mol. However, we can see that the distortion energy curves are very similar along the entire coordinate, and it is actually the different interaction curves that generate the barrier difference. In the case of R = Ph and R = 4- $\text{C}_6\text{H}_4\text{OMe}$, the interaction energies are very similar along the reaction pathway, both -11.9 kcal/mol at their respective TS. The higher overall distortion for Ph in addition to its later transition state leads to the (electronic energy) activation barrier of Ph (25.0 kcal/mol) being 5.1 kcal/mol higher than for 4- $\text{C}_6\text{H}_4\text{OMe}$ (19.9 kcal/mol).

The simplicity of this interpretation might motivate considering distortion and interaction as merely steric and electronic parameters, respectively. However, this is not a correct interpretation. There are also important contributions from electronic effects in the calculation of the distortion energy. For example, the bonding of the amido nitrogen to the zirconium center is through a hybridized p-orbital of N, and the trigonal planar binding geometry (sp^2 -like) is distorted to pyramidal (sp^3 -like) to accommodate CO₂ in the TS. For R = Me, this distortion has little effect on the overall electronic structure, but this same distortion leads to broken aromaticity for R = Ph, drastically increasing the distortion energy of this complex (see Supporting Information Section S4 for HOMO visualization). The interaction energy should also be considered with nuance because steric factors impact the bonding capability of the mutually orienting fragments.

Partial Charge and Geometry Analysis. The analysis of partial atomic charges provides further understanding of the observed differences in reactivity at the molecular level (Figure 7), including alternative parameters that could be computed to demonstrate TS lateness with less computational expense than calculating entire IRC trajectories, which might not always be possible for complex systems. The difference in partial atomic charges between intermediates is indicative of a shift in electron localization. As shown in Figure 7, the CM5 charges on nitrogen become more positive when progressing from intermediate 1a to TS1a (-0.61 to -0.54) or 1b to TS1b

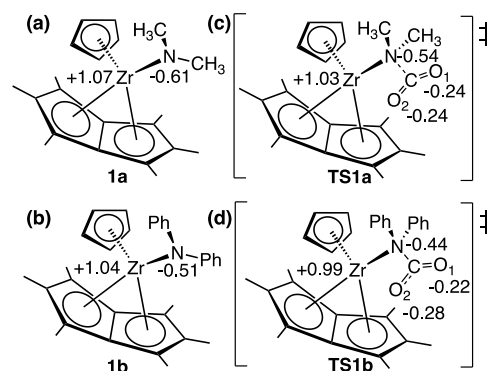


Figure 7. Comparison of the CM5 partial atomic charges at reactive atoms on the (a) dimethyl amido intermediate, 1a, (b) dimethyl amido RL TS, TS1a, (c) diphenyl amido intermediate, 1b, and (d) diphenyl amido RL TS, TS1b.

(-0.51 to -0.44) since electron density is transferred from the amine to CO₂ (Table 1). Both complexes show a change in the partial charge on nitrogen of +0.07.

Table 1. CM5 Atomic Partial Charges [a.u.] of Key Atoms in TS1a and TS1b

atom	TS1a	TS1b	Δ
N	−0.537	−0.442	+0.095
C	+0.364	+0.359	−0.005
O1	−0.244	−0.220	+0.024
O2	−0.243	−0.277	−0.034
$\Delta\text{O (O2−O1)}$	+0.001	−0.057	−0.058

An interesting asymmetry arises when examining the charge distribution of the carbamate oxygens in the TS. The partial charges on the oxygens in methyl-substituted TS1a are equivalent, which indicates a CO₂-like electronic distribution in that TS. However, in phenyl-substituted TS1b, the oxygen partial charges are unbalanced. The oxygen proximal to Zr has more negative partial charge, indicating an additional electron density on this oxygen and suggesting that TS1b has a product-like electronic distribution. The discrepancy between the atomic partial charges in these TSs reveals that the methyl substituent corresponds with an early TS, and incorporation of the more electron-withdrawing phenyl substituent results in a later TS.

To further examine this result, the optimized geometries of TS1a and TS1b were compared. In TS1b, the N–C bond length is shorter, the C–O bond lengths are not equal, and the O–C–O bond angle is contracted (Figure 8, Table 2).

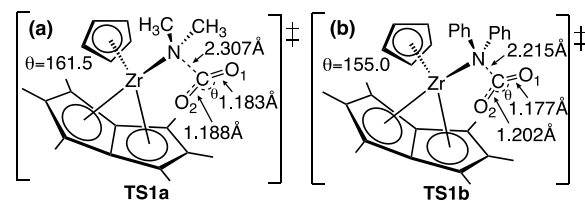


Figure 8. Geometries of the CO₂ insertion TS for (a) methyl- and (b) phenyl-substituted Pn^*Zr analogues. Going from TS1a to TS1b, the C–N bond is shortened by 0.092 Å, the C–O2 bond is lengthened by 0.014 Å, and the O1–C–O2 angle contracted by 6.5°. These geometric changes all indicate a later TS for R = Ph.

Table 2. Values of Key Geometric Parameters in TS1a and TS1b

parameter	TS1a	TS1b	Δ
Zr–N (Å)	2.252	2.380	+0.128
N–CO ₂ (Å)	2.307	2.215	–0.092
C–O1	1.183	1.177	–0.006
C–O2	1.188	1.202	+0.014
Zr–O2 (Å)	3.391	2.623	–0.768
O–C–O	161.5	155.0	–6.5

These distortions are reported on by the greater ΔE_{dist} of TS1b and are indicators of a later TS with a carbamate-like geometry. The Zr–N and C–N bond lengths across substituent Hammett parameters are shown in Table S4 and demonstrate the effect of a changing electronic character on TS lateness. TS1c, which has the strongest EWG, has the largest ΔE_{dist} of CO₂ (20.0 kcal/mol), the shortest N–CO₂ bond length in the TS (1.96 Å), and the most bent CO₂ angle (148.4°). This is consistent with 1c having the latest TS for CO₂ activation because of the stronger electron-withdrawing effect of CH₂F. Metrical parameters for TS1c and TS1d are reported in Supporting Information Section S5.

CONCLUSIONS

We have investigated the origin of the reactivity difference toward CO₂ activation of two permethylpentene (η^8 -C₈Me₆ = Pn*) zirconium cyclopentadienyl (mono)amido complexes. Our DFT analysis shows that changing the substituents on the amido ligand from methyl to phenyl delays the rate-limiting TS and increases the activation barrier.

The nuanced contribution of steric and electronic effects was elucidated using the distortion–interaction method. Steric effects primarily control the trend in distortion, and smaller substituents show systematically lower distortion energies. Electronic effects primarily control interactions, and more electron-donating substituents have systematically more negative interaction energies. The balance of these effects leads to the TS location of complexes with EWGs to be shifted later along the PES to regions with larger distortion energies; the sum of distortion and interaction at this location gives a higher activation barrier. In the case of PnZr with Me and Ph amido substituents, the combined effect of an electron-donating, sterically unhindered substituent is to give an earlier TS with a lower activation barrier.

These results explain the observed reactivity difference between analogous Pn*ZrCp(NR₂) complexes which can aid the design of group 4 metal complexes for CO₂ activation. The quantitative analysis enabled by the distortion–interaction method highlights the importance of considering both steric and electronic aspects of design for facile CO₂ activation catalysts.

ASSOCIATED CONTENT

Supporting Information

The Supporting Information is available free of charge at <https://pubs.acs.org/doi/10.1021/acs.inorgchem.2c03533>.

Benchmarking results, analysis of IRC endpoints, distortion–interaction analyses of TS1c–d, HOMO visualizations and bonding analysis, partial charge and geometric analysis, sample input files, and coordinates of optimized geometries (PDF)

AUTHOR INFORMATION

Corresponding Author

Victor S. Batista – Department of Chemistry, Yale University, New Haven, Connecticut 06520, United States; Yale Energy Sciences Institute, Yale University, West Haven, Connecticut 06516, United States; orcid.org/0000-0002-3262-1237; Email: victor.batista@yale.edu

Authors

Daniel Chabeda – Department of Chemistry, Yale University, New Haven, Connecticut 06520, United States; orcid.org/0000-0003-0152-7528

H. Ray Kelly – Department of Chemistry, Yale University, New Haven, Connecticut 06520, United States; Yale Energy Sciences Institute, Yale University, West Haven, Connecticut 06516, United States; orcid.org/0000-0003-3811-0662

Patrick L. Holland – Department of Chemistry, Yale University, New Haven, Connecticut 06520, United States; orcid.org/0000-0002-2883-2031

Complete contact information is available at:

<https://pubs.acs.org/doi/10.1021/acs.inorgchem.2c03533>

Notes

The authors declare no competing financial interest.

ACKNOWLEDGMENTS

This work was supported by the U.S. Department of Energy (DOE), Chemical Sciences, Geosciences, and Biosciences Division, Office of Basic Energy Science under the contract DE-FG02-07ER15909 (V.S.B.). We also acknowledge a generous allocation of high-performance computing time from NERSC.

REFERENCES

- (1) Bresciani, G.; Biancalana, L.; Pampaloni, G.; Marchetti, F. Recent Advances in the Chemistry of Metal Carbamates. *Molecules* **2020**, *25*, 3603.
- (2) Moreno, J. J.; Hooe, S. L.; Machan, C. W. DFT Study on the Electrocatalytic Reduction of CO₂ to CO by a Molecular Chromium Complex. *Inorg. Chem.* **2021**, *60*, 3635–3650.
- (3) Benson, E. E.; Kubiak, C. P.; Sathrum, A. J.; Smieja, J. M. Electrocatalytic and homogeneous approaches to conversion of CO₂ to liquid fuels. *Chem. Soc. Rev.* **2009**, *38*, 89–99.
- (4) Senftle, T. P.; Carter, E. A. The Holy Grail: Chemistry Enabling an Economically Viable CO₂ Capture, Utilization, and Storage Strategy. *Acc. Chem. Res.* **2017**, *50*, 472–475.
- (5) Darensbourg, D. J. Making plastics from carbon dioxide: Salen metal complexes as catalysts for the production of polycarbonates from epoxides and CO₂. *Chem. Rev.* **2007**, *107*, 2388–2410.
- (6) Das, D.; Bhanage, B. M. Double Carbonylation Reactions: Overview and Recent Advances. *Adv. Synth. Catal.* **2020**, *362*, 3022–3058.
- (7) Hamilton, E. A.; Kilpatrick, A. F. R.; Turner, Z. R.; Fraser, D. A. X.; Buffet, J. C.; O'Hare, D. CO₂ activation by permethylpentene amido zirconium complexes. *Dalton Trans.* **2021**, *50*, 4494–4498.
- (8) Vagner, J.; Qu, H. C.; Hrubby, V. J. Peptidomimetics, a synthetic tool of drug discovery. *Curr. Opin. Chem. Biol.* **2008**, *12*, 292–296.
- (9) Ghosh, A. K.; Brindisi, M. Organic Carbamates in Drug Design and Medicinal Chemistry. *J. Med. Chem.* **2015**, *58*, 2895–2940.
- (10) Riemer, D.; Hirapara, P.; Das, S. Chemoselective Synthesis of Carbamates using CO₂ as Carbon Source. *ChemSusChem* **2016**, *9*, 1916–1920.
- (11) Schilling, W.; Das, S. Transition Metal-Free Synthesis of Carbamates Using CO₂ as the Carbon Source. *ChemSusChem* **2020**, *13*, 6246–6258.

- (12) Bickelhaupt, F. M.; Houk, K. N. Analyzing Reaction Rates with the Distortion/Interaction-Activation Strain Model. *Angew. Chem., Int. Ed.* **2017**, *56*, 10070–10086.
- (13) Bickelhaupt, F. M. Understanding reactivity with Kohn-Sham molecular orbital theory: E2-S_N2 mechanistic spectrum and other concepts. *J. Comput. Chem.* **1999**, *20*, 114–128.
- (14) Fernández, I.; Bickelhaupt, F. M. The activation strain model and molecular orbital theory: understanding and designing chemical reactions. *Chem. Soc. Rev.* **2014**, *43*, 4953–4967.
- (15) Wolters, L. P.; Bickelhaupt, F. M. The activation strain model and molecular orbital theory. *Wiley Interdiscip. Rev.: Comput. Mol. Sci.* **2015**, *5*, 324–343.
- (16) Ess, D. H.; Houk, K. N. Distortion/Interaction energy control of 1,3-dipolar cycloaddition reactivity. *J. Am. Chem. Soc.* **2007**, *129*, 10646–10647.
- (17) Ess, D. H.; Houk, K. N. Theory of 1,3-dipolar cycloadditions: Distortion/interaction and frontier molecular orbital models. *J. Am. Chem. Soc.* **2008**, *130*, 10187–10198.
- (18) Vummaleti, S. V. C.; Talarico, G.; Nolan, S. P.; Cavallo, L.; Poater, A. Mechanism of CO₂ Fixation by Ir-I-X Bonds (X = OH, OR, N, C). *Eur. J. Inorg. Chem.* **2015**, *2015*, 4653–4657.
- (19) Truscott, B. J.; Kruger, H.; Webb, P. B.; Bühl, M.; Nolan, S. P. The Mechanism of CO₂ Insertion into Iridium(I) Hydroxide and Alkoxide Bonds: A Kinetics and Computational Study. *Chem.—Eur. J.* **2015**, *21*, 6930–6935.
- (20) Vadivelu, P.; Suresh, C. H. Metal- and Ligand-Assisted CO₂ Insertion into Ru-C, Ru-N, and Ru-O Bonds of Ruthenium(II) Phosphine Complexes: A Density Functional Theory Study. *Inorg. Chem.* **2015**, *54*, 502–512.
- (21) Aguilar, N.; Atilhan, M.; Aparicio, S. Single atom transition metals on MoS₂ monolayer and their use as catalysts for CO₂ activation. *Appl. Surf. Sci.* **2020**, *534*, 147611.
- (22) Blaziak, K.; Tzeli, D.; Xantheas, S. S.; Uggerud, E. The activation of carbon dioxide by first row transition metals (Sc–Zn). *Phys. Chem. Chem. Phys.* **2018**, *20*, 25495–25505.
- (23) Ha, N. N.; Ha, N. T. T.; Van Khu, L. V.; Cam, L. M. Theoretical study of carbon dioxide activation by metals (Co, Cu, Ni) supported on activated carbon. *J. Mol. Model.* **2015**, *21*, 322.
- (24) Pan, Y. X.; Liu, C. J.; Wiltowski, T. S.; Ge, Q. F. CO₂ adsorption and activation over gamma-Al₂O₃-supported transition metal dimers: A density functional study. *Catal. Today* **2009**, *147*, 68–76.
- (25) Grice, K. A. Carbon dioxide reduction with homogenous early transition metal complexes: Opportunities and challenges for developing CO₂ catalysis. *Coord. Chem. Rev.* **2017**, *336*, 78–95.
- (26) Smieja, J. M.; Kubiak, C. P. Re(bipy-tBu)(CO)₃Cl-improved Catalytic Activity for Reduction of Carbon Dioxide: IR-Spectroelectrochemical and Mechanistic Studies. *Inorg. Chem.* **2010**, *49*, 9283–9289.
- (27) Schmeier, T. J.; Nova, A.; Hazari, N.; Maseras, F. Synthesis of PCP-Supported Nickel Complexes and their Reactivity with Carbon Dioxide. *Chem.—Eur. J.* **2012**, *18*, 6915–6927.
- (28) Frisch, M. J.; Trucks, G. W.; Schlegel, H. B.; Scuseria, G. E.; Robb, M. A.; Cheeseman, J. R.; Scalmani, G.; Barone, V.; Petersson, G. A. *Gaussian 16*, Revision C.01; Gaussian, Inc.: Wallingford CT, 2019.
- (29) Perdew, J. P.; Burke, K.; Ernzerhof, M. Generalized gradient approximation made simple. *Phys. Rev. Lett.* **1996**, *77*, 3865–3868.
- (30) Becke, A. D. Density-functional thermochemistry. III. The role of exact exchange. *J. Chem. Phys.* **1993**, *98*, 5648–5652.
- (31) Lee, C. T.; Yang, W. T.; Parr, R. G. Development of the Colle-Salvetti Correlation-Energy Formula into a Functional of the Electron-Density. *Phys. Rev. B: Condens. Matter Mater. Phys.* **1988**, *37*, 785–789.
- (32) Stephens, P. J.; Devlin, F. J.; Chabalowski, C. F.; Frisch, M. J. Ab-initio calculation of vibrational absorption and circular-dichroism spectra using density-functional force fields. *J. Phys. Chem.* **1994**, *98*, 11623–11627.
- (33) Chai, J. D.; Head-Gordon, M. Long-range corrected hybrid density functionals with damped atom-atom dispersion corrections. *Phys. Chem. Chem. Phys.* **2008**, *10*, 6615–6620.
- (34) Weigend, F. Accurate Coulomb-fitting basis sets for H to Rn. *Phys. Chem. Chem. Phys.* **2006**, *8*, 1057–1065.
- (35) Grimme, S.; Ehrlich, S.; Goerigk, L. Effect of the Damping Function in Dispersion Corrected Density Functional Theory. *J. Comput. Chem.* **2011**, *32*, 1456–1465.
- (36) Grimme, S.; Antony, J.; Ehrlich, S.; Krieg, H. A consistent and accurate ab initio parametrization of density functional dispersion correction (DFT-D) for the 94 elements H–Pu. *J. Chem. Phys.* **2010**, *132*, 154104.
- (37) Ditchfield, R.; Hehre, W. J.; Pople, J. A. Self-consistent molecular-orbital methods. 9. Extended Gaussian-type basis for molecular-orbital studies of organic molecules. *J. Chem. Phys.* **1971**, *54*, 724–728.
- (38) Hehre, W. J.; Ditchfield, R.; Pople, J. A. Self-Consistent Molecular Orbital Methods. XII. Further Extensions of Gaussian-Type Basis Sets for Use in Molecular Orbital Studies of Organic Molecules. *J. Chem. Phys.* **1972**, *56*, 2257–2261.
- (39) Hariharan, P. C.; Pople, J. A. Influence of polarization functions on orbital hydrogenation energies. *Theor. Chim. Acta* **1973**, *28*, 213–222.
- (40) Spitznagel, G. W.; Clark, T.; von Ragué Schleyer, P. V.; Hehre, W. J. Efficient diffuse function-augmented basis-sets for anion calculation. IV. An evaluation of the performance of diffuse function-augmented basis sets for 2nd row elements, Na–Cl. *J. Comput. Chem.* **1987**, *8*, 1109–1116.
- (41) Andrae, D.; Haussermann, U.; Dolg, M.; Stoll, H.; Preuss, H. Energy-adjusted ab initio pseudopotentials for the second and third row transition elements: Molecular test for M2 (M=Ag, Au) and MH (M=Ru, Os). *Theor. Chim. Acta* **1991**, *78*, 247–266.
- (42) Krishnan, R.; Binkley, J. S.; Seeger, R.; Pople, J. A. Self-consistent molecular orbital methods. 20. Basis set for correlated wave-functions. *J. Chem. Phys.* **1980**, *72*, 650–654.
- (43) Frisch, M. J.; Pople, J. A.; Binkley, J. S. Self-consistent molecular-orbital methods 25. Supplementary functions for Gaussian basis sets. *J. Chem. Phys.* **1984**, *80*, 3265–3269.
- (44) Weigend, F.; Ahlrichs, R. Balanced basis sets of split valence, triple zeta valence and quadruple zeta valence quality for H to Rn: Design and assessment of accuracy. *Phys. Chem. Chem. Phys.* **2005**, *7*, 3297–3305.
- (45) Miertuš, S.; Scrocco, E.; Tomasi, J. Electrostatic interaction of a solute with a continuum - a direct utilization of ab initio molecular potentials for the prevision of solvent effects. *Chem. Phys.* **1981**, *55*, 117–129.
- (46) Miertuš, S.; Tomasi, J. Approximate evaluations of the electrostatic free-energy and internal energy changes in solution processes. *Chem. Phys.* **1982**, *65*, 239–245.
- (47) Marenich, A. V.; Jerome, S. V.; Cramer, C. J.; Truhlar, D. G. Charge Model 5: An Extension of Hirshfeld Population Analysis for the Accurate Description of Molecular Interactions in Gaseous and Condensed Phases. *J. Chem. Theory Comput.* **2012**, *8*, 527–541.
- (48) Hirshfeld, F. L. Bonded-atom fragments for describing molecular charge-densities. *Theor. Chim. Acta* **1977**, *44*, 129–138.
- (49) Wu, J. G.; Green, J. C.; Hazari, N.; Hruszkewycz, D. P.; Incarvito, C. D.; Schmeier, T. J. The Reaction of Carbon Dioxide with Palladium-Allyl Bonds. *Organometallics* **2010**, *29*, 6369–6376.
- (50) Kilpatrick, A. F. R.; Green, J. C.; Cloke, F. G. N. The Reductive Activation of CO₂ Across a Ti=Ti Double Bond: Synthetic, Structural, and Mechanistic Studies. *Organometallics* **2015**, *34*, 4816–4829.